

Studying the black widow pulsars PSR J0312–0921 and PSR J1627+3219 in the optical and X-rays

A. V. Bobakov^{1*}, A. Kirichenko^{2,1}, S. V. Zharikov², D. A. Zyuzin¹,
A. V. Karpova¹, Yu. A. Shibanov¹, T. Begari³

¹ Ioffe Institute, 26 Politekhnicheskaya, St. Petersburg, 194021, Russia

² Instituto de Astronomía, Universidad Nacional Autónoma de México, Apdo. Postal 877, Ensenada, Baja California, México, 22800

³ American Association of Variable Star Observers, 185 Alewife Brook Parkway, Suite 410, Cambridge, MA 02138, USA

Received ..., 2025; accepted ..., 2025

ABSTRACT

Context. PSR J0312–0921 and PSR J1627+3219 are black widow pulsars with orbital periods of 2.34 and 3.98 hours. They were recently detected in the radio and γ -rays.

Aims. Our goals are to estimate the fundamental parameters of both binary systems and their components.

Methods. We performed first phase-resolved multi-band photometry of both objects with the 10.4-m Gran Telescopio Canarias and fitted the obtained light curves with a model assuming direct heating of the companion by the pulsar. Archival X-ray data obtained with the *Swift* and *XMM-Newton* observatories were also analysed.

Results. For the first time, we firmly identified both systems in the optical. Their optical light curves show a rather symmetric single peak per orbital period and a peak-to-peak amplitude of ≥ 2 mag. We also identified the X-ray counterpart to J1627+3219, while for J0312–0921 we set an upper limit on the X-ray flux.

Conclusions. We estimated the masses of the pulsars, companion temperatures and masses, Roche lobe filling factors, orbital inclinations, and the distances to both systems. PSR J0312–0921 has a very light ($\approx 0.02 M_{\odot}$) companion which possibly has one of the lowest (≈ 1600 K) ‘night-side’ temperatures among the known black widow systems. We found that the distances to J0312–0921 and J1627+3219 are about 2.5 and 4.6 kpc, respectively. This likely explains their faintness in X-rays. The X-ray spectrum of PSR J1627+3219 can be described by the power-law model, and its parameters are compatible with those obtained for other black widows.

Key words. binaries: close – stars: neutron – pulsars: individual: PSR J0312–0921 – pulsars: individual: PSR J1627+3219

1. Introduction

Black widows (BW) form a subclass of the so-called ‘spider’ systems, which are binary millisecond pulsars (MSPs) with short orbital periods ($P_b \lesssim 1$ d) and low-mass companions ($M_c \lesssim 0.05 M_{\odot}$ for BWs; Roberts 2013). The companion in these systems is heated and evaporated by the pulsar high-energy radiation and the wind of relativistic particles, which can cause eclipses of the pulsar radio emission. BW pulsars are recycled by accretion of matter and angular momentum from main-sequence companion stars during a low-mass X-ray binary (LMXB) stage (Bisnovatyi-Kogan & Komberg 1974; Alpar et al. 1982). In addition, BWs were proposed as potential progenitors of isolated MSPs (e.g., Ginzburg & Quataert 2020; Guo et al. 2022). However, the formation pathway of such systems is not yet completely clear (Chen et al. 2013; Benvenuto et al. 2014; Ginzburg & Quataert 2021; Guo et al. 2024).

To date, 49 confirmed BWs have been discovered in the Galactic field, mainly through observations in the radio and γ -rays (Koljonen & Linares 2025). These observations can provide information on the source position, pulsar mass function, spin period, binary period, and distance. Optical studies of BW systems are crucial for obtaining other fundamental parameters such as the companion surface temperature distribution, its Roche-lobe filling factor, and irradiation efficiency. Moreover, they are useful for measuring the masses of binary components, orbital inclination,

and distance, especially in cases where these parameters cannot be constrained well from radio or γ -ray timing observations alone. Recent optical studies of a sample of BWs provided valuable constraints on their system parameters (Draghis et al. 2019; Mata Sánchez et al. 2023; Bobakov et al. 2024).

The BW pulsars PSR J0312–0921 and PSR J1627+3219 (hereafter J0312 and J1627) were recently discovered with the Green Bank and Five hundred meter Aperture Spherical radio Telescopes, respectively, during searches of unassociated *Fermi* Large Area Telescope (LAT) γ -ray sources (Tabassum et al. 2021; Saz Parkinson 2021; Li et al. 2022). Pulsations with the pulsars’ spin periods were also detected in γ -rays (Smith et al. 2023). The parameters of the systems are presented in Table 1. We note that the J0312 orbital period 2.34 h is one of the shortest among those of the known BWs (see, e.g., Swihart et al. 2022).

Here we report the results of the first multi-band optical observations of J0312 and J1627 with the 10.4-m Gran Telescopio Canarias (GTC). In addition, we analysed archival X-ray observations carried out with the *Swift* X-Ray Telescope (XRT) and *XMM-Newton* observatory. The paper is organised as follows: optical observations and data reduction are described in Sec. 2 and the modelling of the light curves – in Sec. 3. Analysis of the X-ray data is presented in Sec. 4. Discussion and conclusions are given in Sec. 5.

* E-mail: bobakov_alex@mail.ru

Table 1. The J0312 and J1627 parameters.

PSR	J0312	J1627
Right ascension α (J2000)	03 ^h 12 ^m 06 ^s .21465615(2)	16 ^h 27 ^m 52 ^s .9985(5)
Declination δ (J2000)	−09°21′56″.55324461(5)	+32°18′26″.643(8)
Galactic longitude l , deg	191.510	52.970
Galactic latitude b , deg	−52.378	43.209
Spin period P , ms	3.7043355330862(3)	2.1828338203418(5)
Spin period derivative \dot{P} , s s ^{−1}	1.9723(6)×10 ^{−20}	5.478(4)×10 ^{−21}
Orbital period P_b , d	0.0974588765(11)	0.165880827(4)
Dispersion measure DM, pc cm ^{−3}	20.5	—
Distance D_{YMW} , kpc	0.82	4.47
Characteristic age $\tau_c \equiv P/2\dot{P}$, Gyr	3.0	6.3
Observed spin-down luminosity \dot{E} , erg s ^{−1}	1.5×10 ³⁴	2.1×10 ³⁴
Minimum companion mass $M_{\text{c, min}}$, M _⊙	0.009	0.022
Mass function f_M , M _⊙	3.9×10 ^{−7}	6×10 ^{−6}
P.m. in RA direction $\mu_\alpha \cos \delta$, mas yr ^{−1}	31.7±1.2	1.6±1.4
P.m. in Dec direction μ_δ , mas yr ^{−1}	8.9±3.0	−2.8±1.5

Notes. Parameters are taken from the web page of the Third *Fermi* LAT catalog of γ -ray pulsars (https://fermi.gsfc.nasa.gov/ssc/data/access/lat/3rd_PSR_catalog/3PC_HTML/) and the Australia Telescope National Facility Pulsar catalogue (Manchester et al. 2005; <https://www.atnf.csiro.au/people/pulsar/psrcat/>). Numbers in parentheses denote 1σ uncertainties relating to the last significant digit quoted. P.m. \equiv proper motion. D_{YMW} is the DM distance calculated using the YMW16 (Yao et al. 2017) model for the distribution of free electrons in the Galaxy. For J1627, the value is taken from Smith et al. (2023). The spin-down luminosity is calculated assuming the canonical moment of inertia of 10^{45} g cm². The minimum companion mass is calculated assuming a system inclination of $i = 90^\circ$ and a canonical pulsar mass of $M_p = 1.35 M_\odot$ (similarly to e.g., Koljonen & Linares 2025). The mass function for J0312 is calculated from the orbital parameters.

Table 2. Log of observations.

Date yy/mm/dd	Filter	Exposure time, s	Airmass	Seeing, arcsec
J0312				
2023/10/10	g'	200 × 18	1.3–1.4	0.6–0.9
	r'	180 × 20		
2023/10/11	r'	180 × 18	1.3–1.6	0.7–0.8
	i'	120 × 18		
J1627				
2024/07/29	u_s	121.6 × 126	1.0–2.0	0.7–2.5
	g_s	60.8 × 252		
	r_s	60.8 × 252		
	i_s	60.8 × 252		
	z_s	121.6 × 126		

2. Optical observations and data reduction

2.1. J0312

The phase-resolved photometric observations¹ of the J0312 field were performed during two observing runs in October 2023 in the Sloan g' , r' and i' bands with the Optical System for Imaging and low Resolution Integrated Spectroscopy (OSIRIS+) instrument².

¹ Proposal GTC14-23BMEX, PI A. Kirichenko

² <https://www.gtc.iac.es/instruments/osiris+/osiris+.php>

The OSIRIS+ field of view (FoV) is $7'8 \times 7'8$ with a pixel scale of $0''.254$ in the standard 2×2 binning mode.

The observations were carried out under photometric weather conditions. To avoid effects from CCD defects, we used $5''$ dithering between the individual exposures. Each observing run (with durations of about 2.7 h and 2.3 h) covered approximately one orbital period of the system. To optimise the efficiency of observations, in the first run we used the alternating g' and r' bands, while in the second run the BW period was covered in the r' and i' bands. The log of observations is presented in Table 2 and the r' -band image of the pulsar field is shown in the top panel of Fig. 1, where the variability of the pulsar companion is demonstrated in the insets.

Standard data reduction, including bias subtraction and flat-fielding, was performed using the Image Reduction and Analysis Facility (IRAF) package. We applied the L.A.Cosmic algorithm (van Dokkum 2001) to remove cosmic-ray events. For astrometric referencing, we used a single 180-s r' -band image and a set of stars from the *Gaia* DR3 Catalogue (Gaia Collaboration et al. 2023). The formal rms uncertainties of the fit were $\Delta\alpha \lesssim 0''.13$ and $\Delta\delta \lesssim 0''.14$.

For the photometric calibration, we used the Sloan photometric standard SA 112-805 (Smith et al. 2002) observed during the same nights as the target. Accounting for the extinction coefficients $k_{g'} = 0.15(2)$, $k_{r'} = 0.07(1)$, and $k_{i'} = 0.04(1)$ (Cabrerá-Lavers et al. 2014), we calculated the zero points $Z_{g'} = 28.07(2)$, $Z_{r'} = 28.09(1)$ (2023/10/10), $Z_{r'} = 28.02(1)$ (2023/10/11), and $Z_{i'} = 27.58(1)$. We verified these zero points using a set of stars from the Panoramic Survey Telescope and Rapid Response System Data Release (DR) 2 catalogue (Pan-STARRS; Flewelling et al. 2020, see Fig. 1) and short exposures obtained in each band for the calibration purposes. The 3σ detection limits during the

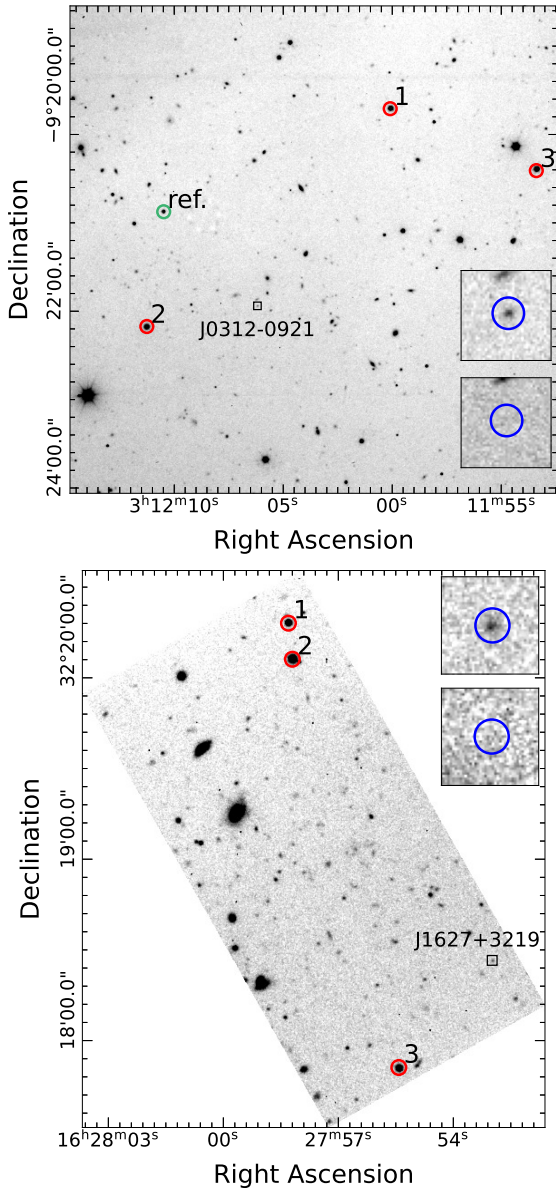


Fig. 1. Optical images of the fields of the two pulsars. *Top panel:* $3:05 \times 3:05$ image of the J0312 field obtained with the GTC/OSIRIS in the r' band. *Bottom panel:* $2:8 \times 1:4$ FoV of the GTC/HiPERCAM in the g_s band containing J1627. The pulsars' vicinities are shown by the boxes and enlarged in the insets to demonstrate the maximum (top) and minimum (bottom) brightness phases of their companions, whose positions are marked by blue circles. The positions of stars used for the photometric calibration are marked by red circles. In the upper panel, the star used to account for the changing weather conditions is shown by the green circle. For J1627, for this purpose we used the same stars as for the photometric calibration.

observations were $g' \approx 26.5$ mag, $r' \approx 25.75$ – 25.9 mag, and $i' \approx 24.6$ – 24.8 mag. We note that all magnitudes presented in this paper are in the AB system.

We used the optimal extraction algorithm (Naylor 1998), to extract the target light curves and applied a differential technique to eliminate the variations due to changing weather conditions using a non-variable bright field star from the Pan-STARRS DR2 catalogue as a reference (Fig. 1, top). Its magnitude scatters were $\lesssim 0.05$ mag during the runs.

2.2. J1627

The phase-resolved multi-band observations of the J1627 field were performed on 2024 July 29³ with the HiPERCAM instrument⁴ (Dhillon et al. 2016, 2018, 2021) simultaneously in five (u_s , g_s , r_s , i_s , and z_s) high-throughput ‘Super’ SDSS filters. The HiPERCAM FoV is $2:8 \times 1:4$, with the $0:16$ pixel scale in the 2×2 binning mode. The observations were performed under photometric weather conditions. The log of observations is presented in Table 2. The total duration was 4.4 h covering one orbital period.

We performed standard data reduction including bias subtraction, flat-field correction and z_s -band fringe removal following the pipeline manual⁵. An example of the g_s -band individual image is presented in Fig. 1, bottom. The pulsar companion variability is demonstrated in the two insets.

Using the optimal extraction algorithm (Naylor 1998), we measured instrumental magnitudes of the counterpart and three stars in the FoV whose magnitudes are available in the SDSS DR18 catalogue (Almeida et al. 2023). To avoid centroiding problems of the companion during its faint brightness stages, its position was fixed relative to the nearest star when the source was in its maximum brightness phase. We performed photometric calibration using the GTC atmospheric extinction coefficients $k_{u_s} = 0.48$, $k_{g_s} = 0.17$, $k_{r_s} = 0.1$, $k_{i_s} = 0.05$, and $k_{z_s} = 0.05$ (Dhillon et al. 2021) and the spectrophotometric standards Feige110 and WD1606+422 (Oke 1990; Kilic et al. 2020) observed during the same night as the target. To eliminate possible systematic errors and to account for photometric zero-point variations during the observation, we used the technique described in Honeycutt (1992) and stable Pan-STARRS stars (Fig. 1) whose magnitude scatters were $\lesssim 0.05$ mag during the observing run. The measured magnitudes of the latter were compared with their catalogue values. This allowed us to verify the calibration, which resulted in the final zero-points $Z_{u_s} = 27.62 \pm 0.05$, $Z_{g_s} = 28.87 \pm 0.01$, $Z_{r_s} = 28.46 \pm 0.02$, $Z_{i_s} = 28.00 \pm 0.02$, $Z_{z_s} = 27.67 \pm 0.02$. Due to weather conditions, the detection limits varied in the ranges of $u_s \approx 24.6$ – 25.6 mag, $g_s \approx 24.9$ – 25.7 mag, $r_s \approx 24.3$ – 25.2 mag, $i_s \approx 23.9$ – 24.7 mag, and $z_s \approx 23.6$ – 24.4 mag.

The light curves of J1627 were obtained in the g_s , r_s , i_s , and z_s bands while in the u_s -band its brightness was below the HiPERCAM sensitivity limit.

3. Optical light curves and the system parameters

The resulting barycentre-corrected light curves of J0312 and J1627 folded with their orbital periods (Table 1) are presented in Fig. 2. To estimate the system parameters, we fitted the light curves using the direct heating model consisting of a neutron star (NS) as the primary irradiating a low-mass companion as the secondary. The emission of each surface element of the secondary is approximated by a black-body spectrum with an effective temperature varying from element to element. We note that for J1627 we used only g_s -, r_s - and i_s -band points since the model cannot describe data in the wider spectral range from the g_s to z_s band using the black body approximation for an element irradiation. Details of the model can be found in Zharikov et al. (2013, 2019) and Kirichenko et al. (2024). The model takes into account the irradiation of the secondary $T_d = (T_n^4 + \sigma^{-1} \cos(\alpha_n) \Omega K_{\text{irr}})^{1/4}$ as it

³ Proposal GTC6-24AMEX, PI A. Kirichenko

⁴ <http://www.gtc.iac.es/instruments/hipercam/hipercam.php>

⁵ <https://cygnus.astro.warwick.ac.uk/phsaap/hipercam/docs/html/>

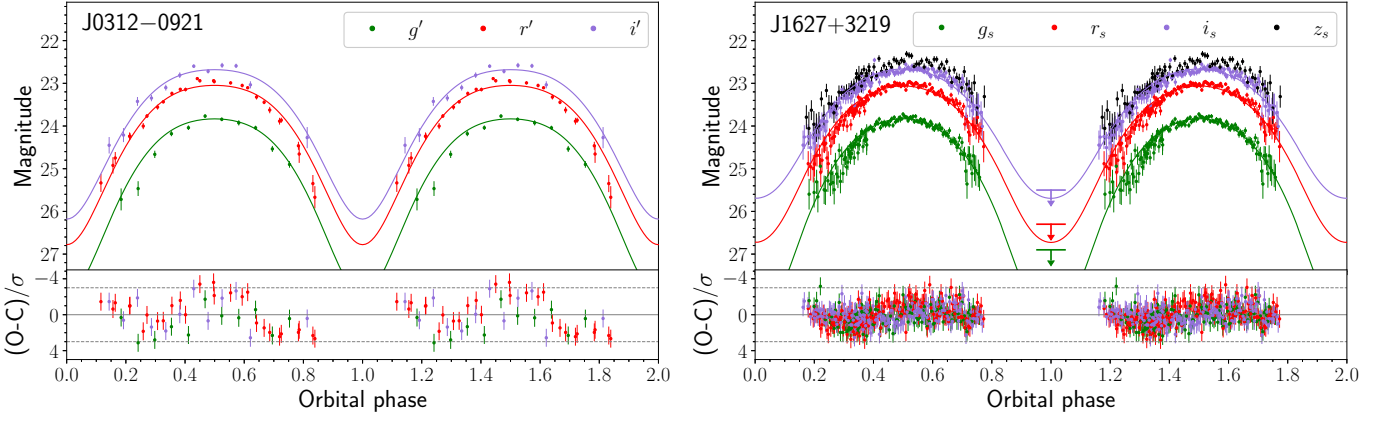


Fig. 2. Light curves of the J0312 (left) and J1627 (right) folded with the orbital periods and the best-fitting models (solid lines). Two periods are shown for clarity. The orbital phases $\phi = 0.0$ correspond to the minima of the models' brightness. Sub-panels demonstrate residuals calculated as the difference between the observed (O) and calculated (C) magnitudes for each data point in terms of the magnitude error, σ . Dashed lines correspond to 3σ levels.

Table 3. The light-curve fitting results.

Fitted parameters	J0312	J1627
Pulsar mass M_p , M_\odot	$2.6^{+0.4}_{-0.9}$	$2.7^{+0.3}_{-1.0}$
Mass ratio $q = M_c/M_p$	0.008(1)	0.017(2)
Distance D , kpc	2.5(2)	4.6(2)
Reddening $E(B - V)$, mag	0.18(4)	0.051(25)
'Night-side' temperature T_n , K	1600^{+200}_{-600}	2730(300)
Inclination i , deg	43^{+13}_{-7}	54^{+10}_{-4}
Roche lobe filling factor f_x	$0.94^{+0.05}_{-0.10}$	0.71(7)
Irradiation factor K_{irr} , $10^{20} \text{ erg cm}^{-2} \text{ s}^{-1} \text{ sr}^{-1}$	0.8(2)	2.4(2)
$\chi^2/\text{d.o.f.}$	205/44	570/448
Derived parameters		
Companion mass M_c , M_\odot	0.02(1)	0.04(2)
Companion radius $R_{c,x}$, R_\odot	0.14(2)	0.21(2)
Companion radius $R_{c,y}$, R_\odot	0.11(2)	0.15(2)
Max 'day-side' temp. T_d^{max} , K	5940(200)	5570(80)
Irradiation efficiency η	0.31(8)	0.64(5)

Notes. Irradiation efficiencies η are calculated using the observed spin-down luminosities from Table 1. $R_{c,x}$ and $R_{c,y}$ are the radii of the ellipsoidal companion. The former is along the line passing through the centres of the binary components. $K_{\text{irr}} = \frac{\eta \dot{E}}{4\pi^2 R_p^2}$, where $R_p = 12 \text{ km}$ is the pulsar radius. D.o.f. \equiv degrees of freedom. The errors of the derived

parameters were calculated as $\Delta f = \sqrt{\sum_{i=1}^n \left(\frac{\partial f}{\partial x_i} \bigg|_{x_i=x_i^{\text{best}}} \Delta x_i \right)^2}$, where f is the function corresponding to the derived parameter, n is the number of fitted parameters, and Δx_i is the absolute value of the maximum error of the parameter x_i at its best value.

was described in Zharikov et al. (2019)⁶, the quadratic law of the limb-darkening with coefficients from Claret et al. (2012, 2013,

⁶ α_n is the angle between the incoming flux and the normal to the secondary surface, $\Omega = \pi R_p^2/a^2$ is the solid angle from which the pulsar is visible from the secondary, and a is the orbit separation, K_{irr} is the effective

equation 2 therein), and the gravity darkening from Prša (2018, equation 5.4 therein).

The fitted parameters are the interstellar reddening $E(B - V)$, the distance D , the pulsar mass M_p , the component mass ratio q , the orbit inclination i , the effective irradiation factor K_{irr} defining heating of the companion, the companion Roche lobe filling factor f defined as a ratio of distances from the centre of mass of the secondary to the star surface and to the Lagrange point L_1 , and the companion 'night-side' temperature T_n . We used the mass functions from the radio observations (Table 1) to link the companion mass M_c (or the mass ratio $q = M_c/M_p$), M_p , and i . The minimum of the χ^2 function was determined using the gradient descent method. This approach was preferred as it considerably reduces the computational effort required for the minimisation. The parameter uncertainties were calculated following the method proposed by Lampton et al. (1976). The results are presented in Table 3 and the best-fitting models for both objects are shown by solid lines in Fig. 2.

To check whether the model predictions near the J1627 minimum brightness phase are adequate, we combined 20 images at $\phi \approx 0.00 \pm 0.05$. Nevertheless, the target was not detected in any band. The corresponding detection limits were $g_s \approx 26.9$ mag, $r_s \approx 26.3$ mag and $i_s \approx 25.5$ mag which is compatible with the model. For J0312, the number of data points near the minimum brightness phase is not enough to significantly improve the detection limits derived in Sec. 2.1.

4. X-ray data

The J0312 and J1627 fields were observed with *Swift*/XRT several times between 2010 and 2019 with total exposure times of 5.4 and 8.1 ks, respectively. No statistically significant sources were detected at the pulsars' positions. Using the Living *Swift*-XRT Point Source (LSXPS) Upper limit server⁷ (Evans et al. 2023), we derived the 3σ upper limits on the sources' count rates $\text{CR}^{\text{J0312}} = 2.2 \times 10^{-3} \text{ cts s}^{-1}$ and $\text{CR}^{\text{J1627}} = 1.2 \times 10^{-3} \text{ cts s}^{-1}$. This corresponds to the unabsorbed fluxes in the 0.5–10 keV range $F_X^{\text{J0312}} \approx 7.9 \times 10^{-14} \text{ erg s}^{-1} \text{ cm}^{-2}$ and $F_X^{\text{J1627}} \approx 3 \times 10^{-14} \text{ erg s}^{-1} \text{ cm}^{-2}$. Here we assume a power law (PL) model with the

tive irradiation factor of the secondary, and σ is the Stefan-Boltzmann constant.

⁷ <https://www.swift.ac.uk/LSXPS/ulserv.php>

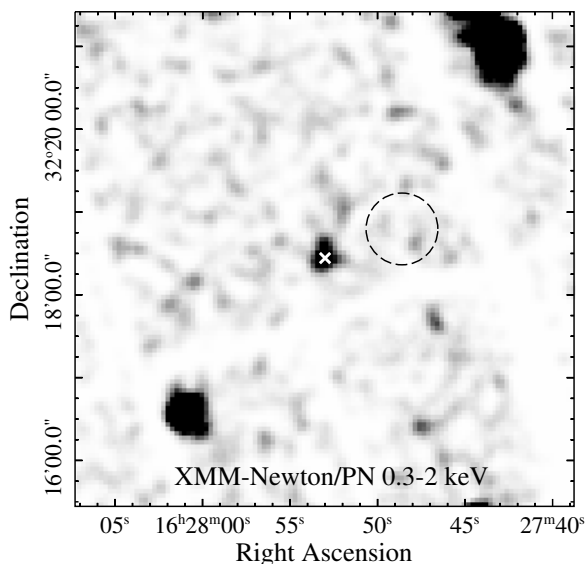


Fig. 3. $6' \times 6'$ *XMM-Newton*/PN image of the J1627 field in the 0.3–2 keV band. The ‘X’ symbol marks the pulsar timing position from Table 1. The dashed circle shows the region chosen for the background extraction.

photon index $\Gamma = 2.5$, which is the average value for the BW family (Swihart et al. 2022). The absorbing column densities were $N_{\text{H}}^{\text{J0312}} = 1.6 \times 10^{21} \text{ cm}^{-2}$ and $N_{\text{H}}^{\text{J1627}} = 4.5 \times 10^{20} \text{ cm}^{-2}$. They were calculated using the reddening values obtained for J0312 and J1627 from the optical fits (Table 3) and the empirical relation from Foight et al. (2016).

The J1627 field was also observed⁸ with *XMM-Newton* on 2023 February 10 with duration of 38.5 ks. The European Photon Imaging Camera-Metal Oxide Semiconductor (EPIC-MOS) and EPIC-pn (PN hereafter) detectors were operated in the full frame mode with the thin filter. The *XMM-Newton* Science Analysis Software (XMM-SAS) v.22.1.0 was utilised for data reduction. The data were reprocessed using the *emproc* and *epproc* routines. Unfortunately, the high-energy light curves extracted from the FoVs of detectors showed a significant number of strong background flares. We filtered them out applying the *espfilt* task. This resulted in effective exposure times of 18.4, 18.8, and 11.2 ks for the MOS1, MOS2, and PN detectors, respectively. Using the *edetect_chain* tool⁹ and data from all detectors, we performed source detection. A weak X-ray source, the likely counterpart of J1627, was detected at the pulsar timing position (Fig. 3). Its coordinates are $\alpha_{\text{X}} = 16^{\text{h}}27^{\text{m}}53^{\text{s}}.15$ and $\delta_{\text{X}} = 32^{\circ}18'26''.0$ and position uncertainty is $2''$ (the latter combines the statistical uncertainty of $1''.6$ and absolute astrometry accuracy for *XMM-Newton*/EPIC¹⁰ of $1''.2$). We also found that the source is not detected in the MOS1 or MOS2 data alone likely due to lower efficiency of the MOS detectors in the soft energy band ($\lesssim 2 \text{ keV}$) in comparison with the PN camera.

We extracted the source spectrum from the PN data using $10''$ -radius aperture around its position using the *evselect* tool. For the background, the $26''$ -radius circle was chosen (Fig. 3). The redistribution matrix and ancillary response files were created

by the *rmfgen* and *arfgen* tasks. We obtained 30.6 net counts in the 0.2–10 keV band and grouped the spectrum to ensure at least 1 count per energy bin. It was fitted in the X-Ray Spectral Fitting Package (XSPEC) v.12.15.0 (Arnaud 1996), applying the *W*-statistics appropriate for Poisson data with Poisson background¹¹ and the PL model. The *tbabs* model with the *wilm* abundances (Wilms et al. 2000) was also included to account for the interstellar absorption. The absorbing column density was fixed at the value mentioned above. As a result, we derived the photon index $\Gamma = 3.3 \pm 0.5$, the unabsorbed flux in the 0.5–10 keV band and $W/\text{d.o.f.} = 25/24$ (uncertainties are at 1σ confidence). The flux value is in agreement with the upper limit obtained from the *Swift* data.

5. Discussion and conclusions

We carried out the first multi-band time-series optical photometry of J0312 and J1627. The light curves of both systems are rather symmetric and have one peak per orbital period with a peak-to-peak amplitude of $\gtrsim 2 \text{ mag}$, which is typical for the BW family (Swihart et al. 2022; Mata Sánchez et al. 2023). The curves can be described by the direct heating model. We note that there is a hint of some deviation from the model seen in the residuals for both objects. It can be caused by different effects such as, e.g., cold spots on the donor star surface (Clark et al. 2021), heating by the intrabinary shock (Romani & Sanchez 2016) or heat redistribution over the companion surface via convection and diffusion (Kandel & Romani 2023; Voisin et al. 2020). However, the significance of these possible features is low, and further investigations are necessary to confirm or reject them.

The companions in both systems have very low masses ($M_{\text{c}}^{\text{J0312}} = 0.02 M_{\odot}$ and $M_{\text{c}}^{\text{J1627}} = 0.04 M_{\odot}$), which is typical for the BW population (Swihart et al. 2022). Their temperatures are also compatible with those obtained for BWs (Mata Sánchez et al. 2023), and among them the J0312 companion may have one of the lowest ($\approx 1600 \text{ K}$) ‘night-side’ temperatures.

For a significant number of spider pulsars, DM distances are compatible with the parallax distances or are lower than them (see fig. 5 in Koljonen & Linares 2023). The same situation occurs for our targets: for J1627 the distance provided by the optical fit (4.6 kpc) is close to the DM one (4.5 kpc), while for J0312 it is much greater (2.5 vs 0.8 kpc).

The reddening value for J1627 obtained from the optical fit (Table 3) is in agreement with the maximal $E(B - V) \approx 0.04 \text{ mag}$ derived from the 3D dust map of Green et al. (2019). For J0312, the maximal $E(B - V)$ is about 0.1 mag, which is less than the best-fitting value. However, the map inspection shows that the interstellar medium in the J0312 circumstance is rather non-uniform, providing $E(B - V)$ up to $\approx 0.2 \text{ mag}$. There are no main-sequence stars at distances $\gtrsim 2.1 \text{ kpc}$, and, the star density in the pulsar field is low. Thus, the map results can be dubious. In addition, the uncertainties of the model reddening are quite large.

The J0312 and J1627 proper motions derived from the radio timing are $\mu^{\text{J0312}} = 33.0 \pm 1.4 \text{ mas yr}^{-1}$ and $\mu^{\text{J1627}} = 3.2 \pm 1.4 \text{ mas yr}^{-1}$. The J1627 transverse velocity corresponding to the distance 4.6 kpc from the optical fit, is $v_t \approx 70 \text{ km s}^{-1}$. This value is compatible with typical binary pulsar velocities, which are mostly lower than 150 km s^{-1} (Hobbs et al. 2005). In contrast, J0312 has a transverse velocity of $\approx 400 \text{ km s}^{-1}$ at 2.5 kpc, which is considerably higher than, e.g., $v_t = 326 \text{ km s}^{-1}$ of the high-velocity MSP PSR B1257+12 (Yan et al. 2013). Moreover, correction for

⁸ ObsID 0902730101, PI P. Saz Parkinson

⁹ <https://www.cosmos.esa.int/web/xmm-newton/sas-thread-src-find>

¹⁰ <https://xmmweb.esac.esa.int/docs/documents/CAL-TN-0018.pdf>.

¹¹ <https://heasarc.gsfc.nasa.gov/xanadu/xspec/manual/XSappendixStatistics.html>

the Shklovskii effect (Shklovskii 1970) and acceleration due to differential Galactic rotation (Nice & Taylor 1995; Lynch et al. 2018) leads to a negative intrinsic \dot{P} value. This implies that either the distance or the proper motion is overestimated. Formally, the DM distance of 0.8 kpc provides an acceptable positive \dot{P} and v_l . However, a smaller distance implies a smaller intrinsic flux of the companion, leading to its unreasonably small radius of $\sim(25\text{--}30)\times 10^3$ km. On the other hand, reliable measurements of the proper motion require a close distance and/or long time base of observations. Dispersion measure variations and timing noise can also lead to inaccurate calculations. For this reason, the J0312 proper motion may be overestimated similar to that of, e.g., BW PSR J1641+8049. An updated timing solution for this pulsar led to a significantly lower proper motion compared to the previous estimate, rejecting the spin-up scenario (Kirichenko et al. 2024).

According to the *Fermi* LAT 14-Year Point Source Catalog DR 4, the J0312 and J1627 fluxes in the 0.1–100 GeV range are $F_\gamma^{J0312} = 5.6(4) \times 10^{-12}$ erg s $^{-1}$ cm $^{-2}$ and $F_\gamma^{J1627} = 4.0(3) \times 10^{-12}$ erg s $^{-1}$ cm $^{-2}$ (Ballet et al. 2023). Using the distances from Table 3 we calculated the corresponding luminosities $L_\gamma^{J0312} = 4.2 \times 10^{33}$ erg s $^{-1}$ and $L_\gamma^{J1627} \approx 10^{34}$ erg s $^{-1}$. The 3σ upper limit on the J0312 X-ray luminosity is $L_X^{J0312} < 5.9 \times 10^{31}$ erg s $^{-1}$. The X-ray luminosity of J1627 is $L_X^{J1627} \approx 1.1 \times 10^{31}$ erg s $^{-1}$. These values are consistent with those of other BWs (Swihart et al. 2022; Koljonen & Linares 2023). The J1627 photon index of ≈ 3.3 is also typical for a BW. It is high enough to suggest the possible presence of a thermal component originating from the heated polar caps, although the low count statistics does not allow us to make definite conclusions.

The γ -ray and X-ray efficiencies calculated using the observed spin-down luminosities for J0312 are $\eta_\gamma^{J0312} = L_\gamma/\dot{E} = 0.28$ and $\eta_X^{J1627} = L_X/\dot{E} < 4 \times 10^{-3}$ and for J1627 – $\eta_\gamma^{J1627} = 0.48$ and $\eta_X^{J1627} = 5 \times 10^{-4}$. While the X-ray efficiencies are reasonable for BWs, the γ -ray and irradiation efficiencies are very high. However, here we used the observed values of the spin-down luminosity, while the intrinsic values can be significantly different. The correction for the acceleration due to differential Galactic rotation is small and does not change critically \dot{E} . The Shklovskii effect for J1627 is also negligible. However, if the pulsars have masses larger than the canonical value of $1.4 M_\odot$, then their true \dot{E} can be essentially higher. For example, for a pulsar radius of 12–13 km and a mass of $1.7 M_\odot$, which is a lower bound for both objects (see Table 3), the intrinsic \dot{E} will be ~ 2 times higher¹².

The next generation of instruments would be useful to better constrain the parameters of the systems.

Acknowledgements. We thank the anonymous referee for useful comments. The work is based on observations made with the Gran Telescopio Canarias (GTC), installed at the Spanish Observatorio del Roque de los Muchachos of the Instituto de Astrofísica de Canarias, on the island of La Palma and on observations obtained with *XMM-Newton*, a ESA science mission with instruments and contributions directly funded by ESA Member States and NASA. This work made use of data supplied by the UK Swift Science Data Centre at the University of Leicester. This work has made use of data from the European Space Agency (ESA) mission *Gaia* (<https://www.cosmos.esa.int/gaia>), processed by the *Gaia* Data Processing and Analysis Consortium (DPAC, <https://www.cosmos.esa.int/web/gaia/dpac/consortium>). Funding for the DPAC has been provided by national institutions, in particular the institutions participating in the *Gaia* Multilateral Agreement. The work of AVB, DAZ and YAS (optical data reduction) was supported by the baseline project FFUG-2024-0002 of the Ioffe Institute. The analysis of the X-ray data by AVK was supported by the Russian Science Foundation project 22-12-00048-P. AK acknowledges the DGAPA-PAPIIT grant IA105024. SVZ acknowledges the DGAPA-PAPIIT grant IN19323. DAZ thanks Pirinem School of Theoretical Physics for hospitality.

References

- Almeida, A., Anderson, S. F., Argudo-Fernández, M., et al. 2023, *ApJS*, 267, 44
 Alpar, M. A., Cheng, A. F., Ruderman, M. A., & Shaham, J. 1982, *Nature*, 300, 728
 Arnaud, K. A. 1996, in *Astronomical Society of the Pacific Conference Series*, Vol. 101, *Astronomical Data Analysis Software and Systems V*, ed. G. H. Jacoby & J. Barnes, 17
 Ballet, J., Bruehl, P., Burnett, T. H., Lott, B., & The Fermi-LAT collaboration. 2023, arXiv e-prints, arXiv:2307.12546
 Benvenuto, O. G., De Vito, M. A., & Horvath, J. E. 2014, *ApJ*, 786, L7
 Bisnovatyi-Kogan, G. S. & Komberg, B. V. 1974, *Soviet Astronomy*, 18, 217
 Bobakov, A. V., Kirichenko, A. Y., Zharikov, S. V., et al. 2024, *A&A*, 690, A173
 Cabrera-Lavers, A., Pérez-García, A., Abril Abril, M., Bongiovanni, A., & Cepa, G. 2014, *Canarian Observatories Updates CUPS*, 3, https://www.gtc.iac.es/instruments/osiris/media/CUPS_BBpaper.pdf
 Chen, H.-L., Chen, X., Tauris, T. M., & Han, Z. 2013, *ApJ*, 775, 27
 Claret, A., Hauschildt, P. H., & Witte, S. 2012, *A&A*, 546, A14
 Claret, A., Hauschildt, P. H., & Witte, S. 2013, *A&A*, 552, A16
 Clark, C. J., Nieder, L., Voisin, G., et al. 2021, *MNRAS*, 502, 915
 Dhillon, V., Dixon, S., Gamble, T., et al. 2018, in *Society of Photo-Optical Instrumentation Engineers (SPIE) Conference Series*, Vol. 10702, *Ground-based and Airborne Instrumentation for Astronomy VII*, ed. C. J. Evans, L. Simard, & H. Takami, 107020L
 Dhillon, V. S., Bezawada, N., Black, M., et al. 2021, *MNRAS*, 507, 350
 Dhillon, V. S., Marsh, T. R., Bezawada, N., et al. 2016, in *Society of Photo-Optical Instrumentation Engineers (SPIE) Conference Series*, Vol. 9908, *Ground-based and Airborne Instrumentation for Astronomy VI*, ed. C. J. Evans, L. Simard, & H. Takami, 99080Y
 Draghici, P., Romani, R. W., Filippenko, A. V., et al. 2019, *ApJ*, 883, 108
 Evans, P. A., Page, K. L., Beardmore, A. P., et al. 2023, *MNRAS*, 518, 174
 Flewelling, H. A., Magnier, E. A., Chambers, K. C., et al. 2020, *ApJS*, 251, 7
 Foight, D. R., Güver, T., Özel, F., & Slane, P. O. 2016, *ApJ*, 826, 66
 Gaia Collaboration, Vallenari, A., Brown, A. G. A., et al. 2023, *A&A*, 674, A1
 Ginzburg, S. & Quataert, E. 2020, *MNRAS*, 495, 3656
 Ginzburg, S. & Quataert, E. 2021, *MNRAS*, 500, 1592
 Green, G. M., Schlafly, E., Zucker, C., Speagle, J. S., & Finkbeiner, D. 2019, *ApJ*, 887, 93
 Guo, Y., Wang, B., & Han, Z. 2022, *MNRAS*, 515, 2725
 Guo, Y., Wang, B., & Li, X. 2024, *MNRAS*, 527, 7394
 Hobbs, G., Lorimer, D. R., Lyne, A. G., & Kramer, M. 2005, *MNRAS*, 360, 974
 Honeycutt, R. K. 1992, *PASP*, 104, 435
 Kandel, D. & Romani, R. W. 2023, *ApJ*, 942, 6
 Kilic, M., Bédard, A., Bergeron, P., & Kosakowski, A. 2020, *MNRAS*, 493, 2805
 Kirichenko, A. Y., Zharikov, S. V., Karpova, A. V., et al. 2024, *MNRAS*, 527, 4563
 Koljonen, K. I. I. & Linares, M. 2023, *MNRAS*, 525, 3963
 Koljonen, K. I. I. & Linares, M. 2025, arXiv e-prints, arXiv:2505.11691
 Lampton, M., Margon, B., & Bowyer, S. 1976, *ApJ*, 208, 177
 Li, D., Wang, P., Hou, X., et al. 2022, *Joint Pulsar Studies with the FAST radio telescope and the Fermi LAT*, https://indico.cern.ch/event/1091305/contributions/5007590/attachments/2530789/4354373/221010_Saz_Parkinson_10thFSymp_opt.pdf
 Lynch, R. S., Swiggum, J. K., Kondratiev, V. I., et al. 2018, *ApJ*, 859, 93
 Manchester, R. N., Hobbs, G. B., Teoh, A., & Hobbs, M. 2005, *AJ*, 129, 1993
 Mata Sánchez, D., Kennedy, M. R., Clark, C. J., et al. 2023, *MNRAS*, 520, 2217
 Naylor, T. 1998, *MNRAS*, 296, 339
 Nice, D. J. & Taylor, J. H. 1995, *ApJ*, 441, 429
 Oke, J. B. 1990, *AJ*, 99, 1621
 Prša, A. 2018, *Modeling and Analysis of Eclipsing Binary Stars: The theory and design principles of PHOEBE*
 Ravenhall, D. G. & Pethick, C. J. 1994, *ApJ*, 424, 846
 Roberts, M. S. E. 2013, in *IAU Symposium*, Vol. 291, *Neutron Stars and Pulsars: Challenges and Opportunities after 80 years*, ed. J. van Leeuwen, 127–132
 Romani, R. W. & Sanchez, N. 2016, *ApJ*, 828, 7
 Saz Parkinson, P. 2021, *The X-ray counterpart of PSR J1627+3219, a new MSP discovered by FAST, XMM-Newton Proposal ID #90273*
 Shklovskii, I. S. 1970, *Soviet Ast.*, 13, 562
 Smith, D. A., Abdollahi, S., Ajello, M., et al. 2023, *ApJ*, 958, 191
 Smith, J. A., Tucker, D. L., Kent, S., et al. 2002, *AJ*, 123, 2121
 Swihart, S. J., Strader, J., Chomiuk, L., et al. 2022, *ApJ*, 941, 199
 Tabassum, S., Ransom, S., Ray, P., et al. 2021, in *43rd COSPAR Scientific Assembly*, Held 28 January - 4 February, Vol. 43, 1208
 van Dokkum, P. G. 2001, *PASP*, 113, 1420
 Voisin, G., Kennedy, M. R., Breton, R. P., Clark, C. J., & Mata-Sánchez, D. 2020, *MNRAS*, 499, 1758
 Wilms, J., Allen, A., & McCray, R. 2000, *ApJ*, 542, 914
 Yan, Z., Shen, Z.-Q., Yuan, J.-P., et al. 2013, *MNRAS*, 433, 162
 Yao, J. M., Manchester, R. N., & Wang, N. 2017, *ApJ*, 835, 29
 Zharikov, S., Kirichenko, A., Zyuzin, D., Shibanov, Y., & Deneva, J. S. 2019, *MNRAS*, 489, 5547
 Zharikov, S., Tovmassian, G., Aviles, A., et al. 2013, *A&A*, 549, A77

¹² Here we applied the formula from Ravenhall & Pethick (1994).